

Suspension Force-Coupling Analysis of Flux-Reversal Bearingless Slice Motor Based on Advanced Magnetic Field Model

Jiayun Liu, Ronghai Qu, *Fellow, IEEE*, Dawei Li, *Senior Member, IEEE*, Wubin Kong, *Member, IEEE*, Tianjie Zou, *Member, IEEE*, Xiaodong Sun, *Senior Member, IEEE*

Abstract—Flux-reversal bearingless slice motor with direct suspension current (DC-FRBLM) is a novel slice bearingless motor. The robust rotor structure of the DC-FRBLM brings benefits including high compactness and ease of manufacturing. However, the disparate frequencies of torque current and suspension currents cause undesirable suspension force-coupling in different radial directions. This feature leads to rotor vibrations and poses challenges for suspension control. To address these issues, an advanced magnetic field model and a suspension decoupling control strategy based on this model are proposed in this paper. The proposed model incorporates a precise double-salient permeance model, accounting for variations in rotor magnetic potential and leakage flux. The accurate calculation of the active radial force is achieved using the Maxwell stress tensor method, which agrees well with the finite element analysis (FEA) results. Then an analysis is conducted to identify the magnetic field components responsible for suspension force-coupling. Furthermore, the decoupling strategy based on the proposed analytical model effectively reduces force fluctuation and mitigates rotor vibrations. Experimental results on a prototype of DC-FRBLM validate the improved levitation performance achieved by the proposed decoupling strategy.

Index Terms—Analytical model, decoupling control, flux reversal, magnetic field, radial force, slice bearingless motor.

I. INTRODUCTION

BEARINGLESS motors combine magnetic levitation bearings and conventional motor, providing advantages such as no pollution, no lubrication, no direct contact rotor and an almost unlimited lifetime [1]. Furthermore, compared to magnetic levitation bearings, bearingless motors exhibit superior characteristics related to cost-effectiveness, reduced weight and simplicity of construction [2]. These unique advantages have gained considerable interest for bearingless motors in applications including bioreactor mixers [3], artificial hearts [4], transportation [5].

Among various types of bearingless motors, the permanent magnet (PM) slice bearingless motor has garnered extensive attention, due to its simple construction and low drive system requirements [6]. Notable research has been conducted to explore different variations of the PM slice bearingless motor, including interior PM bearingless slice motor [7], consequent-pole bearingless motor [8], homopolar bearingless motor [9], Vernier PM motor [10] and flux-reversal bearingless slice motor [11]. The flux-reversal bearingless motor features simple rotor structure and relatively high torque density, granting it an advantage in applications characterized by high operating temperatures or the need for disposable rotors. Based on

the flux-reversal bearingless motor, the novel DC-FRBLM proposed in [12] inherits the benefits of simple rotor structure. Additionally, it adopts a consequent-pole stator design, which mitigates the risk of demagnetization and enables suspension using direct current (DC). This design also achieves decoupling of the suspension current control from the rotor angle. However, the difference in frequency between the torque current and the suspension current in the DC-FRBLM results in amplified suspension force-coupling in x - y axis, leading to a degradation in levitation performance.

Various advanced control methods have been employed in bearingless motors to address the challenge of force-coupling [13]–[16]. These control strategies rely on accurate suspension force models, as it plays a crucial role in enhancing suspension control performance and simplifying control strategy design. Consequently, obtaining an accurate suspension force model for the DC-FRBLM is imperative to improve the levitation performance. The suspension force model is typically derived from the magnetic field model [2]. According to [17], magnetic field models can be categorized as numerical, 1-D analytical and 2-D analytical models. While numerical methods, such as FEA, and 2-D analytical methods, such as magnetic network [18] and subdomain model [19], provide precise predictions of the magnetic field, they lack clear physical meaning, making them less suitable for control strategy design. Conversely, 1-D analytical methods, including Magneto-motive force (MMF)-permeance model [20] and equivalent magnetic circuit model [21] are widely employed in bearingless motors analysis [16], [20] thanks to the concise expressions and clear physical interpretations.

However, the widely used simplifying 1-D magnetic field model, such as the MMF-permeance model, exhibits limited accuracy when applied to the DC-FRBLM due to its double-salient air-gap structure and complex magnetic field harmonics. To further improve the accuracy, this paper proposes an advanced magnetic field model based on the MMF-permeance model. The proposed model incorporates additional details, including an accurate representation of the double-salient air-gap permeance, variation in rotor magnetic potential, and the consideration of leakage flux. Based on the proposed model, the radial force is accurately calculated, and a decoupling strategy is designed to enhance the performance of suspension control. The subsequent sections of this article are organized as follows: Section II introduces the topology and operation method of the DC-FRBLM. In Section III, the advanced

magnetic field model is derived and verified using the FEA model. Section IV focuses on the calculation of the active radial force. The designed decoupling strategy based on the analytical model to address force-coupling in the x - y axis is also presented in Section IV. Furthermore, Section V verifies the effectiveness of the decoupling strategy through experiments. Finally, the conclusions are summarized in Section VI.

II. TOPOLOGY AND OPERATION PRINCIPLE

As depicted in Fig. 1, the proposed DC-FRBLM comprises a stator with six slots and a rotor with ten teeth. The electromagnetically-active components of the DC-FRBLM include concentrated windings, a slice rotor and a consequent-pole stator. The stator teeth are mounted with PMs featuring consistent polarities on each tooth and alternating polarities on adjacent teeth. Moreover, Fig. 1 provides a definition of the α - β coordinate system, the d - q coordinate system and the x - y coordinate system. Fig. 2 illustrates the principle of passive stabilization in both the axial and tilt directions. The x - y axis remains stationary, aligning with the α - β axis, which represents the direction of suspension current. Meanwhile, the d - q axis, signifying the direction of torque current, rotates at an electrical frequency corresponding to ten pole-pairs. The phase currents in Fig. 1 can be defined as (1):

$$\begin{cases} i_M = i_{S,M} + i_{T,M} \\ i_{S,M} = I_S \cos\left(\varphi_S + \frac{2m\pi}{3}\right) \\ i_{T,M} = I_T \cos\left(\omega_e t + \varphi_T - \frac{m\pi}{3}\right) \end{cases} \quad (1)$$

where i_M is the current of the M^{th} phase, with $M = A, B, \dots, F$ corresponding to $m = 0, 1, \dots, 5$. I_S, I_T are current amplitude of the suspension current and torque current, φ_S, φ_T are the current phase and ω_e is the electrical frequency of torque current.

The suspension current, which is DC, generates a non-uniform magnetic field, resulting in the creation of a controllable suspension force, as shown in Fig. 3. Driven by the phase current, the primary air-gap flux density B_m consists of three distinct components as:

$$B_m(\theta_s, t) = B_{pm}(\theta_s, t) + B_S(\theta_s, t) + B_T(\theta_s, t) \quad (2)$$

where θ_s is the mechanical angle. B_{pm}, B_S and B_T are the flux density of the air-gap produced by the PM, $i_{S,M}$ and $i_{T,M}$.

According to [1], the controllable radial force is generated through the harmonic combinations of magnetic field with pole pairs differing by one, all rotating at the same speed. In the proposed DC-FRBLM, B_{pm} comprises odd harmonics which include both static components and rotating components regulated by the rotor teeth. B_S consists of static even harmonics, while B_T comprises rotating odd harmonics. The generation of the controllable radial force is contingent upon the interaction between B_S and the static components of B_{pm} , while the torque is generated through the interplay of the rotating components of B_{pm} and B_T . However, as the controllable radial force relies on the static magnetic field, the presence of the rotating magnetic field induces force fluctuations and coupling along the x - y axis. To minimize the

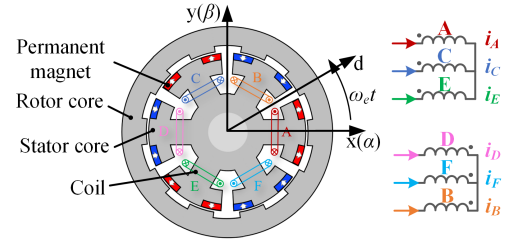


Fig. 1. The structure of the proposed DC-FRBLM.

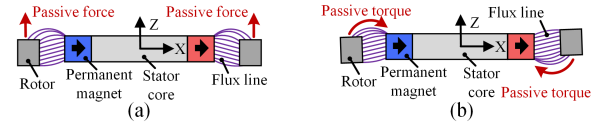


Fig. 2. Passive stabilization. (a) Passive force generation in axial direction. (b) Passive torque generation in tilt direction.

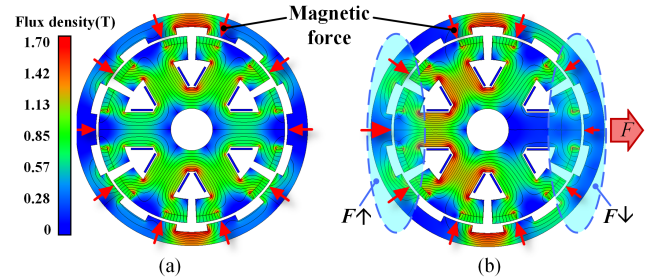


Fig. 3. Flux density distributions and suspension force. (a) Open circuit magnetic field. (b) $I_S = 4.9$ A, $\varphi_S = 0$ deg, $I_T = 0$ A.

adverse effects of force-coupling, it is crucial to obtain an accurate model for the radial force and implement an effective decoupling strategy.

III. ADVANCED MAGNETIC FIELD MODEL

The active radial force of x - y axis can be calculated by the Maxwell stress tensor method as shown in (3). The designed parameters of the DC-FRBLM are defined in Table I.

$$\begin{cases} F_x(\theta_s) = \frac{l_r}{2\mu_0} \int_0^{2\pi} B_m^2(\theta_s, t) \cos\theta_s d\theta_s \\ F_y(\theta_s) = \frac{l_r}{2\mu_0} \int_0^{2\pi} B_m^2(\theta_s, t) \sin\theta_s d\theta_s \end{cases} \quad (3)$$

F_x and F_y are active radial forces in x - y axis. The calculation of radial force relies on the magnetic field analytical model. However, the conventional MMF-permeance model [20] does not suit the DC-FRBLM and tends to result in substantial errors in magnetic field calculation. To improve analytical model accuracy, this section introduces an advanced magnetic field model. For simplification, the following analysis is based on the preconditions [22]:

- 1) Both air-gap flux density, air-gap permeance and MMF keep constantly in the radial direction.
- 2) The permeability of stator and rotor cores is regarded as infinite, hence the potential drop in the core is ignored.

TABLE I
THE KEY PARAMETERS OF THE DESIGNED DC-FRBLM

Parameters	Values	Parameters	Values
Turns of windings per phase, N_s	60	Arc angle of stator iron pole, θ_{fe}	24 deg
Thickness of magnet, d_{pm}	5 mm	Rotor slot depth, d_{rt}	5 mm
Outer radius of stator, r_s	71 mm	Inner radius of rotor, r_r	73 mm
Average radius, r	72 mm	Outer radius of rotor	88.4 mm
Arc angle of magnet, θ_{pm}	15 deg	Arc angle of rotor teeth, θ_{mt}	18 deg
Arc angle of the notch, θ_{no}	6 deg	Stack length, l	10 mm
Number of stator teeth, Z_s	6	Number of rotor teeth, Z_r	10
Relative permeability, μ_r	1.05	Air-gap length, g_0	2 mm
Residual flux density of magnets, B_{r0}	1.07 T	Rated torque	0.79 N·m
Rated speed	400 rpm	Rated force	25.7 N
Rated current	6.5 A		

A. Air-gap Permeance

DC-FRBLM is double-salient, and the expression of its air-gap permeance Λ can be written as:

$$\Lambda(\theta_s, t) = \frac{\mu_0}{\delta_r(\theta_s, t) + \delta_s(\theta_s) - g_0} \quad (4)$$

where δ_s and δ_r are equivalent air-gap lengths of the slotted stator and rotor. Furthermore, (4) can be expanded as:

$$\Lambda(\theta_s, t) = \frac{\mu_0}{g_0} k_{sr}(\theta_s, t) \lambda_r(\theta_s, t) \lambda_s(\theta_s) \quad (5a)$$

$$k_{sr}(\theta_s, t) = \frac{1}{\lambda_s(\theta_s) + \lambda_r(\theta_s, t) - \lambda_r(\theta_s, t) \lambda_s(\theta_s)} \quad (5b)$$

$$\lambda_s(\theta_s) = g_0 / \delta_s(\theta_s), \lambda_r(\theta_s, t) = g_0 / \delta_r(\theta_s, t) \quad (5c)$$

where λ_s and λ_r are relative permeance of slotted stator and rotor. To facilitate the analysis, only half of the period of λ_s and λ_r is taken into account. The air-gap in Fig. 4(a) is divided into three regions by the red dash line, and the influence of the notch is ignored. In **regions I and III**, λ_s remains constant, while in **region II**, it varies due to the impact of the stator tooth edge. The variation of λ_s in region II is neglected in regular model which leads to error in B_{pm} calculation of DC-FRBLM. The path of λ_s in region II forms a 90-degree bend, and the maximum radius of the quarter arc is constrained to $0.5g_0$. The expression of δ_s can be written as:

$$\delta_s(\theta_s) = \begin{cases} g_0 & 0 \leq \theta_s \leq \theta_{s0} \\ g_0 + \left(\frac{\pi}{2} - 1\right) r_s (\theta_s - \theta_{s0}) & \theta_{s0} < \theta_s \leq \theta_{s1} \\ \frac{\pi}{4} g_0 + r_s (\theta_s - \theta_{s0}) & \theta_{s1} < \theta_s \leq \theta_{s2} \\ g_0 + d_{pm} / \mu_r & \theta_{s2} < \theta_s \leq \frac{\pi}{Z_s} \end{cases} \quad (6)$$

$$\begin{cases} \theta_{s0} = 0.5\theta_{fe} - \theta_0, \theta_{s1} = 0.5g_0 / r_s + \theta_{s0} \\ \theta_{s2} = \theta_{s0} + \frac{d_{pm}}{\mu_r r_s} + \left(1 - \frac{\pi}{4}\right) \frac{g_0}{r_s}, \theta_0 = 0.25g_0 / r_s \end{cases} \quad (7)$$

where θ_0 is the fringe angle of permeance model. The boundary angle between region I and II is θ_{s0} , and the boundary angle between regions II and III is θ_{s2} . The similar analysis can be performed on δ_r , giving:

$$\delta_r(\theta_r) = \begin{cases} g_0 & 0 \leq \theta_r \leq \theta_{r0} \\ g_0 + \left(\frac{\pi}{2} - 1\right) r_r (\theta_r - \theta_{r0}) & \theta_{r0} < \theta_r \leq \theta_{r1} \\ \frac{\pi}{4} g_0 + r_r (\theta_r - \theta_{r0}) & \theta_{r1} < \theta_r \leq \theta_{r2} \\ g_0 + d_{rt} & \theta_{r2} < \theta_r \leq \frac{\pi}{Z_r} \end{cases} \quad (8)$$

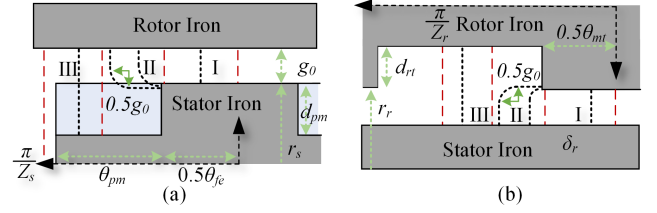


Fig. 4. Permeance path of the air-gap, black short dashed lines indicate the shortest permeance path. The light blue area indicates the PMs which is neglected temporarily. (a) Only stator slotting. (b) Only rotor slotting.

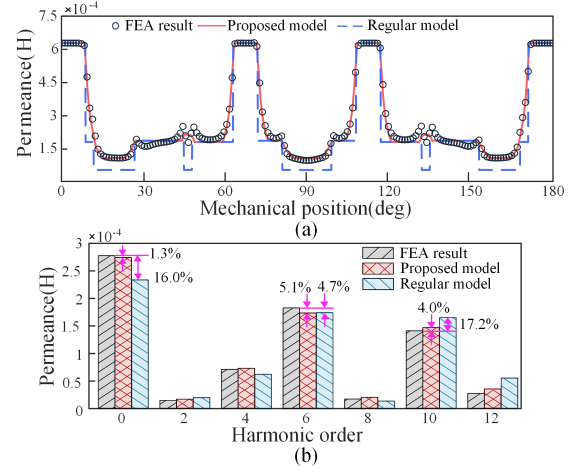


Fig. 5. Air-gap permeance analytical model. (a) Waveforms. (b) Harmonic spectra.

$$\begin{cases} \theta_{r0} = 0.5\theta_{mt} - \theta_0, \theta_{r1} = 0.5g_0 / r_r + \theta_{r0} \\ \theta_{r2} = \theta_{r0} + \frac{d_{rt}}{r_r} + \left(1 - \frac{\pi}{4}\right) \frac{g_0}{r_s}, \theta_r = \Omega t - \theta_s \end{cases} \quad (9)$$

where Ω is the mechanical speed.

In the regular model, the coefficient k_{sr} is typically assumed to be constant, i.e., 1. However, as demonstrated in [22], this simplification can lead to significant deviations in some scenarios. From (5b), it is evident that k_{sr} deviates from 1 when both λ_s and λ_r are not equal to 1. This condition occurs when the PMs are situated opposite to the rotor slots in DC-FRBLM. In this case, the simplifying k_{sr} to 1 would result in substantial errors in the calculation of permeance and flux density, as this region corresponds to the main area of B_{pm} . Consequently, it is essential to consider the precise value of k_{sr} in the proposed model. To facilitate analysis, k_{sr} is transformed to polynomial expression as shown in (10).

$$\begin{cases} k_{sr}(\theta_s, t) \approx 1 - k_{srmax} [\lambda_s + \lambda_r - \lambda_r \lambda_s - 1] \\ k_{srmax} = \frac{(g_0 + d_{rt})(g_0 + d_{pm} / \mu_r)}{g_0(g_0 + d_{rt} + d_{pm} / \mu_r)} \end{cases} \quad (10)$$

The permeance Λ can be expressed as (11) by substituting (5)-(10) to (4). Detailed derivation process and the definition of k_{pr} is shown in Appendix.

$$\Lambda = \sum_{n_s=0}^{\infty} \sum_{n_r=0}^{\infty} k_{pr}(n_r, n_s) \cos(n_r Z_r \theta_r \pm n_s Z_s \theta_s) \quad (11)$$

The waveform and harmonic spectra of Λ obtained from both the proposed model and FEA results are shown in Fig. 5.

And the conventional model of permeance is included for comparison. The result of the proposed model agrees well with the FEA result, especially for DC and 10th harmonic.

B. No-load Air-gap Flux Density

The leakage flux in DC-FRBLM has a negligible impact on the no-load magnetic field, due to the consequent-pole design. To obtain the accurate analytical model, the differential magnetic network method [23] is employed in this section. The differential magnetic circuit associated with N pole magnet of DC-FRBLM is depicted in Fig. 6. For simplicity, the rotor slot is temporarily omitted. The magnetic circuit can be divided into two parts based on the flux direction: the magnet circuit and the iron circuit. The magnet circuit originates from the magnet and primarily encompasses the magnet area. The iron circuit starts from the rotor iron and covers the entire air-gap. It is important to note that the iron circuits of the N and S pole magnets are symmetrically reversed and cancel each other out. Additionally, there are two leakage paths shown in Fig. 6. The main flux of the magnet circuit can be calculated as:

$$\begin{cases} d\Phi_{NT} = \frac{R_m B_r 0}{R_m + R_{gT}} r l d\theta_s \\ d\Phi_m = B_{pm,s} r l d\theta_s = \frac{R_{gT}}{R_g} d\Phi_{NT} \\ R_{gT} = \frac{R_g R_{lN} R_{lN2}}{R_{lN2} R_{lN} + R_{lN2} R_g + R_g R_{lN}} \end{cases} \quad (12)$$

where Φ_{NT} is the total flux of the air-gap, Φ_m is the main flux of the air-gap, R_{gT} is the total flux reluctance of air-gap, R_m is the self-reluctance of the PM, R_g is the reluctance of the average air-gap, R_{lN} and R_{lN2} are the tangent reluctance with different directions on the surface of the stator. A quadratic polynomial is used to fit R_{lN} and R_{lN2} in DC-FRBLM as shown in (13). R_{lN} has a larger value at the junction between the magnet and stator iron, while R_{lN2} has a larger value at the notch. And both R_{lN} and R_{lN2} are nearly zero in the middle of the PMs. The coefficient k_{l1} and k_{l2} are set to 600 and 800, respectfully.

$$\begin{cases} R_g = g_0 / (\mu_0 r l), R_m = d_{pm} / (\mu_r \mu_0 r l) \\ R_{lN} = d_{l1} / (\mu_0 r l), R_{lN2} = d_{l2} / (\mu_0 r l) \\ d_{l1} = k_{l1} r^2 s (\theta_s - \theta_{s0})^2, \theta_p = \frac{1}{2} \theta_{fe} + \theta_{pm} \\ d_{l2} = k_{l2} [r_s (\theta_p - \theta_s) + (\frac{\pi}{2} - 1) g_0]^2 \end{cases} \quad (13)$$

Due to the symmetric design of the stator, the flux density in the middle of the notch is zero. A fractional function of θ_s is used to describe the flux density at the notch. Combining (12)-(13), the flux density in the air-gap of the magnet circuit can be expressed as:

$$B_{pm,s}(\theta_s) = \begin{cases} 0 & 0 < \theta_s \leq \theta_{s0} \\ \frac{B_r 0}{\frac{\mu_r g_0}{d_m} + 1 + \frac{g_0}{d_{l1}} + \frac{g_0}{d_{l2}}} & \theta_{s0} < \theta_s \leq \theta_p \\ B_{g0} \frac{r_s \theta_{no} + g_0}{r_s \theta_{no}} \left(\frac{g_0}{d_N} - \frac{g_0}{d_S} \right) & \theta_p < \theta_s \leq \frac{\pi}{Z_s} \end{cases} \quad (14)$$

$$\begin{cases} d_N = r_s (\theta_s - \theta_p) + g_0, d_S = r_s \theta_{no} + 2g_0 - d_N \\ B_{g0} = \frac{B_r 0 d_{pm}}{(\mu_r g_0 + d_{pm}) + g_0 d_{pm} / d_{l3}} \\ d_{l3} = k_{lN2} (\frac{\pi}{2} - 1)^2 g_0^2 \end{cases} \quad (15)$$

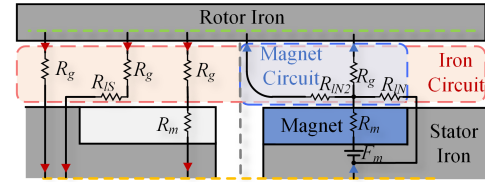


Fig. 6. Differential magnetic circuit of DC-FRBLM with N pole magnet.

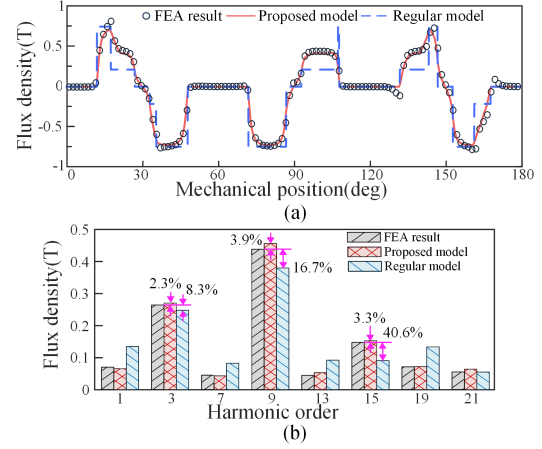


Fig. 7. No-load flux density analytical model. (a) Waveforms of B_{pm} . (b) Harmonic spectra of B_{pm} .

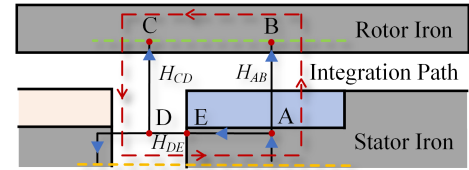


Fig. 8. Integration path for Ampere's law with A phase winding excitation.

where $B_{pm,s}$ is the no-load flux density ignoring the rotor slotted effort. The flux density B_{pm} which further considers the rotor slot effort is calculated by (16).

$$B_{pm}(\theta_s, t) = B_{pm,s} \lambda_r k_{sr} \quad (16)$$

The waveform and harmonic spectra of B_{pm} are shown in Fig. 7. For comparison, the results of the conventional model are also included in Fig. 7. It can be observed that the error of the 3rd, 9th and 15th harmonics between the FEA results and analytical model are within 3.9%.

C. Armature Reaction Field

The armature reaction field is excited by the suspension current and torque current. The corresponding flux density can be obtained as:

$$B_S(\theta_s, t) = F_S \Lambda, \quad B_T(\theta_s, t) = F_T \Lambda \quad (17)$$

where F_S and F_T are the MMF of $i_{S,M}$ and $i_{T,M}$. The MMF distribution per ampere-turn of each phase can be obtained as:

$$A_M(\theta_s) = \sum_{n=1}^{\infty} k_a(n) \cos \left[n \left(\frac{Z_s}{6} \theta_s - \frac{m\pi}{3} \right) \right] \quad (18)$$

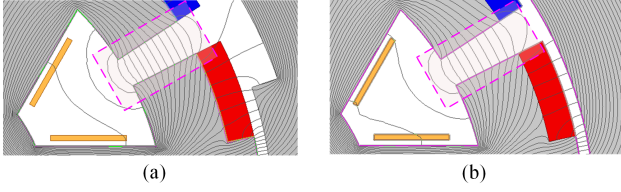


Fig. 9. The flux lines distribution results from FEA. (a) Consider the rotor slot effort. (b) Ignore the rotor slot effort

where $M = A, B, \dots, F$ matches $m = 0, 1, \dots, 5$. The flux lines originating from the stator teeth and entering the rotor represent the main armature reaction field, which play a key role in producing torque and radial force. While the flux lines that begin at one stator tooth and terminate at the adjacent stator tooth are the magnetic leakage, which mainly occurs in the stator notch. The magnetic leakage at the notch causes the variation in MMF of the armature reaction field. The conventional MMF model usually ignores the MMF variation for simplification [20]. To enhance the accuracy of the magnetic model, the MMF model in the notch is obtained by applying Ampere's law to the model depicted in Fig. 8, giving (19). The FEA results of the flux lines distribution at the stator notch are shown in Fig. 9. The flux lines enclosed in the pink dashed box are the magnetic leakage, which remain nearly identical in scenarios both with rotor and without rotor slots. Consequently, it can be inferred that the inclusion or exclusion of rotor slots has minimal impact on the derivation of the MMF model for the armature reaction field. In the subsequent analysis, the rotor is considered as slot-less since the slot effect of the rotor has minimal impact on the MMF model. The magnetic field intensity H_{AB} and H_{DE} can be regarded as constant.

$$H_{AB} - H_{CD} - \frac{(r_s - d_{pm})\theta_{DE}}{g_0 + d_{pm}} H_{DE} = 0 \quad (19)$$

$$\Rightarrow A_{A,(CD)} = \frac{H_{CD}(g_0 + d_{pm})}{N_s I_S} = \frac{\theta_{no} + 2\theta_{02} - \theta_s}{\theta_{no} + 2\theta_{02}}$$

$$\begin{cases} H_{CD} = H_{AB} - \frac{r_s - d_{pm}}{g_0 + d_{pm}} \theta_{DE} H_{DE} \\ H_{AB} = \frac{N_s I_S}{g_0 + d_{pm}}, H_{DE} = \frac{N_s I_S}{(r_s - d_{pm})(\theta_{no} + 2\theta_{02})} \end{cases} \quad (20)$$

$$\theta_{DE} = \theta_s - (0.5\theta_{fe} + \theta_{pm} - \theta_{02}), \theta_{02} = \frac{g_0 + d_{pm}}{2(r_s - d_{pm})} \quad (21)$$

θ_{02} is the fringe angle of the MMF model. Half period of A_A can be expressed as (22). To calculate the coefficient k_a in (18), Fourier expansion is performed on (22), giving (23).

$$A_A(\theta_s) = \begin{cases} 1 - 1/Z_s & 0 < \theta_s \leq \theta_{a1} \\ \frac{\theta_{a2} - \theta_s}{\theta_{gap} + 2\theta_{02}} - 1/Z_s & \theta_{a1} < \theta_s \leq \theta_{a2} \\ -1/Z_s & \theta_{a2} < \theta_s \leq \pi \end{cases} \quad (22)$$

$$\theta_{a1} = 0.5\theta_{fe} + \theta_{pm} - \theta_{02}, \theta_{a2} = \theta_{a1} + \theta_{no} + 2\theta_{02}$$

$$k_a(n) = \frac{2[\cos(n\theta_{a1}) - \cos(n\theta_{a2})]}{\pi n^2(\theta_{no} + 2\theta_{02})} \quad (23)$$

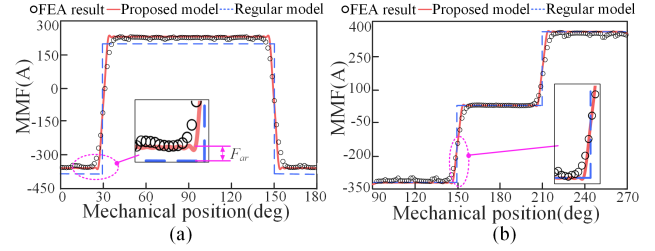


Fig. 10. Waveform of the MMF excited by windings. (a) MMF with $I_S = -6.5$ A, $I_T = 0$ A (b) MMF with $I_S = 0$ A, $I_T = 6.5$ A

The MMF of the armature reaction can be calculated as

$$F_S(\theta_s) = \sum_M N_s A_M i_{S,M} = 3N_s I_S \sum_{n=0}^{\infty} \left\{ \begin{aligned} &k_a(6n+2) \cos\left[\left(n + \frac{2}{6}\right) Z_s \theta_s + \varphi_S\right] \\ &+ k_a(6n+4) \cos\left[\left(n + \frac{4}{6}\right) Z_s \theta_s - \varphi_S\right] \end{aligned} \right\} \quad (24a)$$

$$F_T(\theta_s) = \sum_M N_s A_M i_{T,M} = 3N_s I_T \sum_{n=0}^{\infty} \left\{ \begin{aligned} &k_a(6n+1) \cos\left[\left(n + \frac{1}{6}\right) Z_s \theta_s - \omega_e t - \varphi_T\right] \\ &+ k_a(6n+5) \cos\left[\left(n + \frac{5}{6}\right) Z_s \theta_s + \omega_e t + \varphi_T\right] \end{aligned} \right\} \quad (24b)$$

Considering that $Z_s = 6$, F_S is composed of even harmonics, while F_T is composed of odd harmonics. The permeance Λ comprises even harmonics as well. It can be concluded that the B_S calculated by (17) consists of the 0th harmonic, namely DC component. According to Gauss's theorem, the magnetic potential of the rotor will adjust to offset the DC component, which can be interpreted as an additional MMF F_{ar} added to F_S , as shown in (25). Since the magnetic drop in the rotor core is neglected, F_{ar} remains constant across the air-gap but varies with the rotor position. The accurate flux density of the suspension armature reaction field B_S' can be obtained as (26).

$$\int_0^{2\pi} (B_S + F_{ar}\Lambda) d\theta_s = 0 \Rightarrow F_{ar} = -\frac{\int_0^{2\pi} B_S d\theta_s}{\int_0^{2\pi} \Lambda d\theta_s} = -\frac{B_{S,0}}{\Lambda_0} \quad (25)$$

$$B_S' = B_S + F_{ar}\Lambda \quad (26)$$

The subscript 0 represents the DC component. The waveforms of F_S and F_T are shown in Fig. 10, which proves the correctness of the analysis on F_{ar} .

IV. SUSPENSION FORCE COUPLING ANALYSIS AND DECOUPLING CONTROL STRATEGY

A. Active Suspension Force Analysis

Based on Section II, the active radial force is generated by the combinations of $B_{pm}B_S$ and $B_T B_S$. (3) can be rewritten as (27). By substituting (16), (17) and (26) to (27), the active radial force is expressed as (28) and (29).

$$\begin{cases} F_x(\theta_s) = \frac{lr}{\mu_0} \int_0^{2\pi} (B_{pm}B_S' + B_T B_S') \cos\theta_s d\theta_s \\ F_y(\theta_s) = \frac{lr}{\mu_0} \int_0^{2\pi} (B_{pm}B_S' + B_T B_S') \sin\theta_s d\theta_s \end{cases} \quad (27)$$

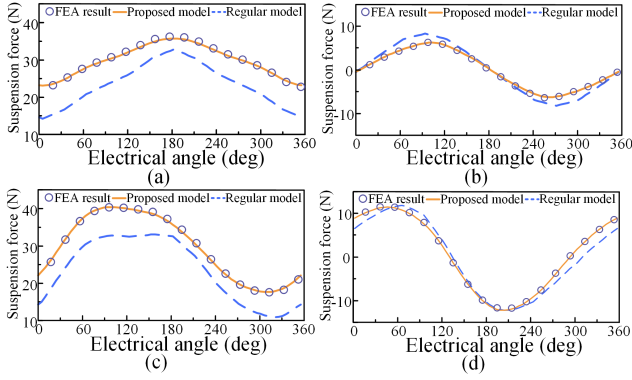


Fig. 11. Active suspension force of FEA results and analytical model with $i_d=i_y=0$ A. (a) x -axis force with $i_x=-6.5$ A, $i_q=0$ A. (b) y -axis force with $i_x=-6.5$ A, $i_q=0$ A. (c) x -axis force with $i_x=-6.5$ A, $i_q=4.9$ A. (d) y -axis force with $i_x=-6.5$ A, $i_q=4.9$ A.

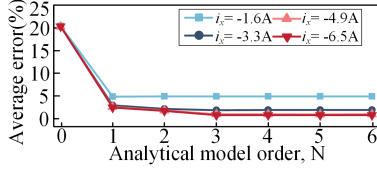


Fig. 12. The average error of x -axis active radial force analytical model with a different order.

$$\begin{bmatrix} F_x \\ F_y \end{bmatrix} = \begin{bmatrix} K_{xx} & K_{xy} \\ K_{yx} & K_{yy} \end{bmatrix} \begin{bmatrix} i_x \\ i_y \end{bmatrix} \quad (28)$$

$$\begin{cases} K_{xx} = \sum_{n=0}^N (k_{xx}(n)c_n + k_{xdx}(n)c_n i_d + k_{xqx}(n)s_n i_q) \\ K_{xy} = \sum_{n=0}^N (k_{xy}(n)s_n + k_{xqy}(n)c_n i_q + k_{xdy}(n)s_n i_d) \\ K_{yx} = \sum_{n=0}^N (k_{yx}(n)s_n + k_{ydx}(n)s_n i_d + k_{yqx}(n)c_n i_q) \\ K_{yy} = \sum_{n=0}^N (k_{yy}(n)c_n + k_{yqy}(n)s_n i_q + k_{ydy}(n)c_n i_d) \end{cases} \quad (29)$$

$c_n = \cos(nZ_r\Omega t)$, $s_n = \sin(nZ_r\Omega t)$

N is the max order of suspension forces considered in the model, i_x and i_y are suspension current in x - y axis, i_d and i_q are torque current in d - q axis.

Table II presents the calculation results of the coefficients in (29). The accuracy of the proposed model is proved via FEA, as shown in Fig. 11. The electrical angle in Fig. 11 is in sync with ω_e . The radial force calculation results based on the proposed analytical model exhibit good agreement with the FEA results, while the results based on conventional model have significant errors, degrading the effect of decoupling strategy. The proposed analytical model exhibiting a notable 20.3% enhancement in the accuracy of suspension force prediction of the DC-FRBLM in x - y axis, compared with the regular magnetic field model. Fig. 12 illustrates the accuracy of the calculation results in relation to parameter N . It can be observed that as N increases, the accuracy of the calculated

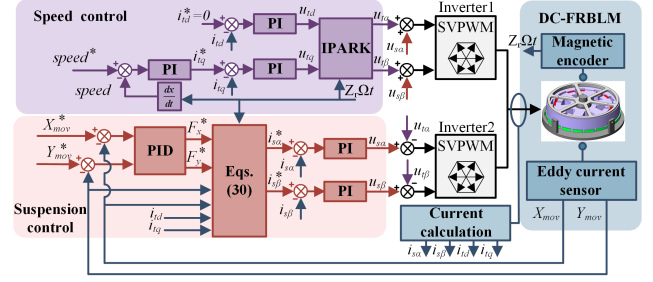


Fig. 13. The control diagram of the DC-FRBLM.

TABLE II
VALUE OF ACTIVE RADIAL FORCE COEFFICIENT

Order	k_{xx}	k_{xy}	k_{yx}	k_{yy}	Unit
0	-4.7049	0	0	-4.7049	N/A
1	0.8946	-0.8946	-0.8946	-0.8946	N/A
2	0.0537	0.0537	0.0537	-0.0537	N/A
3	0.1045	-0.0204	0.0204	0.1045	N/A
Order	k_{xdx}	k_{ydy}	k_{ydx}	k_{xdy}	Unit
0	-0.0776	0	0	-0.0776	N/A ²
1	-0.3439	0.3439	0.3439	0.3439	N/A ²
2	-0.0434	-0.0434	-0.0434	0.0434	N/A ²
3	-0.0029	0	0	-0.0029	N/A ²
Order	k_{yqx}	k_{xqy}	k_{yqy}	k_{ydy}	Unit
0	0	-0.0405	0.0405	0	N/A ²
1	0.3414	0.3414	0.3414	-0.3414	N/A ²
2	0.0447	-0.0447	-0.0447	-0.0447	N/A ²
3	0.0011	-0.0014	0.0014	0.0011	N/A ²

forces improves. The higher-order harmonics of F_x and F_y above the 3rd can be ignored in control for DC-FRBLM.

In Fig. 7(b), the dominant static harmonics in B_{pm} are the 3rd, 9th, and 15th harmonics. And there are rotating harmonics generated by the regulation effort of the rotor teeth in B_{pm} , such as the 1st and 19th harmonics. The average values of F_x and F_y are determined by the static harmonics of B_{pm} and B'_S . While the interaction between B'_S and rotation harmonics of B_{pm} and B_T can cause the force fluctuation, resulting force-coupling in x - y axis. Furthermore, as observed in Fig. 11(a)(c), an increased in i_q exacerbates suspension force-coupling, resulting in a deterioration of suspension control performance and amplified rotor vibration.

B. Control Method

To mitigate the suspension force-coupling in DC-FRBLM, a suspension decoupling strategy based on the proposed analytical model is implemented, as shown in (30). The control block diagram of DC-FRBLM is illustrated in Fig. 13. Suspension force references F_x^* and F_y^* are determined by the proportional-integral-derivative (PID) controller and transformed into suspension current references using (30). As the x - y axis aligns with the α - β axis, no coordinate transformation is required in suspension control. The speed of DC-FRBLM is regulated by a proportional-integral (PI) controller, with i_d is set to zero. Both suspension current and torque current are controlled by PI controllers, and the outputs of the current loops are superimposed on the α - β axis.

$$\begin{cases} i_x^* = \frac{K_{yy}F_x^* - K_{xy}F_y^*}{K_{xx}K_{yy} - K_{xy}K_{yx}} \\ i_y^* = \frac{K_{xx}F_y^* - K_{yx}F_x^*}{K_{xx}K_{yy} - K_{xy}K_{yx}} \end{cases} \quad (30)$$

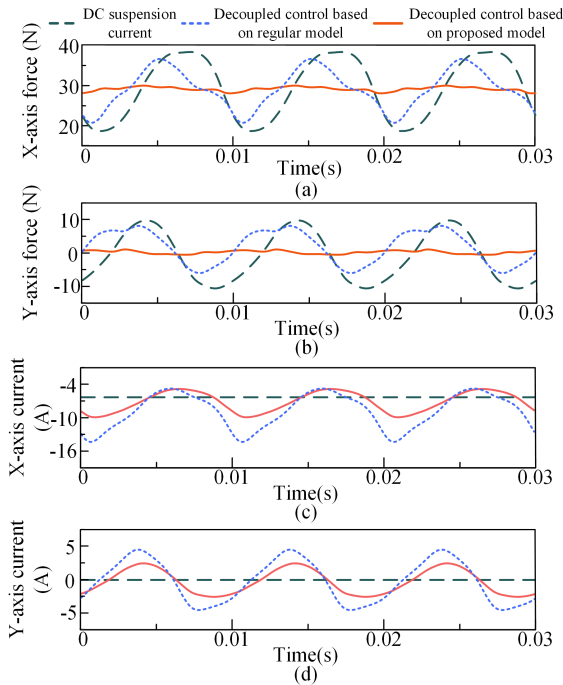


Fig. 14. Simulation results of the active suspension force with decoupling strategy. (a) x -axis active suspension force. (b) y -axis active suspension force. (c) Suspension current of i_x . (d) Suspension current of i_y .

The effectiveness of the decoupling strategy is evaluated using simulation in a FEA model with the suspension current derived from the decoupling strategy as the excitation. In these simulations, the load current i_q was set to 4A. The resulting waveforms of the simulation results, in conjunction with the suspension currents in the x - y axis, are presented Fig. 14. For comparison, the simulation results based on the regular model are also included in Fig. 14. By comparing these different results, it can be learned that through DC suspension currents can produce controllable radial forces, they simultaneously manifest substantial force fluctuations and coupling between the radial force along the x - y axis. In contrast, the proposed strategy can mitigate radial force fluctuations by introducing harmonics currents. It can be observed that the decoupling strategy based on the proposed model significantly reduces the fluctuation of the radial force in the x - y axis compared to the original radial force generated by constant suspension currents. In contrast, the decoupling strategy based on the regular model shows limited effectiveness due to the lower accuracy of the regular model. Furthermore, the calculation of compensatory suspension current is contingent upon the rotor angle position. To ensure an accurate evaluation of the impact of the proposed decoupled strategy, an angle sensor is adopted in Fig. 13 to attain precise rotor angle information.

V. EXPERIMENTAL RESULTS

Experiments were carried out on the test platform to validate the effectiveness of the decoupling strategy, as depicted in Fig. 15. The radial displacement of the DC-FRBLM rotor is limited to 400 μm by the upper and lower motor covers. Two three-phase half-bridges with 10 kHz switching frequency are

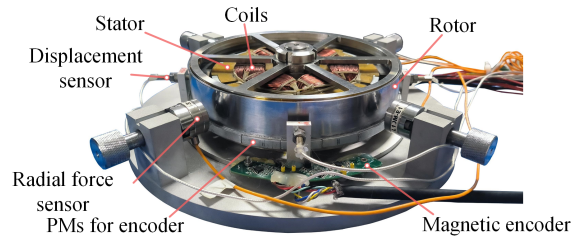


Fig. 15. Experimental setup.

TABLE III
THE CONTROL PARAMETERS

	Levitation loops	Current loops	Speed loops
Proportional gain	6	0.524	12
Integral gain	40	295.3	42
Derivative gain	0.018	-	-
Sampling time	$1 \times 10^{-4} \text{ s}$		$1 \times 10^{-3} \text{ s}$

employed to drive DC-FRBLM, enabling the generation of both suspension and torque currents. Levitation control and torque control are implemented using the TMS320F28335 DSP with a calculation frequency of 10 kHz. The outer surface of the rotor is designed as a detection target to acquire the rotor displacement by eddy current sensors. And a magnetic encoder is employed for rotor position detection. The control parameters are detailed in Table III. To ensure a fair comparison, the following experiments will utilize the same control parameters as specified in Table III.

A radial force measurement experiment was conducted on the DC-FRBLM at standstill to verify the accuracy of the proposed suspension force model. The measured results, shown in Fig. 16, closely match the predictions of the proposed radial force model, which validated the model's high accuracy. The experimental results of Fig. 16 (a) and (b) were obtained under the control conditions of $i_q=0 \text{ A}$, $i_x=-3 \text{ A}$, $i_y=0 \text{ A}$, while those of Fig. 16 (c) and (d) were obtained under the control conditions of $i_q=-2 \text{ A}$, $i_x=-3 \text{ A}$, $i_y=0 \text{ A}$, respectively. The experimental results of Fig. 16 (e) and (f) were obtained under the control conditions of $i_q=-2 \text{ A}$, $i_x=-3 \text{ A}$, $i_y=-3 \text{ A}$. It's noteworthy that, although the results in Fig. 16 (b) and (d) may appear to align with the regular model, the results in Fig. 16 (e) and (f) with i_y injection exhibit differences. The proposed analytical model consistently maintains higher accuracy compared to the regular analytical model, leading to an enhancement in suspension control performance.

The experimental results illustrating the rotor movement during the start-up procedure are presented in Fig. 17. The control procedures are consistent across the waveforms based on different analytic model during the rotor levitation start-up phase. However, variations in the precision of employed analytical models result in different rotor start-up trajectories. Notably, the control strategy based on the proposed analytical model significantly mitigates overshoot in rotor movement compared to the strategy based on the regular analytical model. The response speed of the different waveforms remains similar since the parameters of the PID controller for suspension are

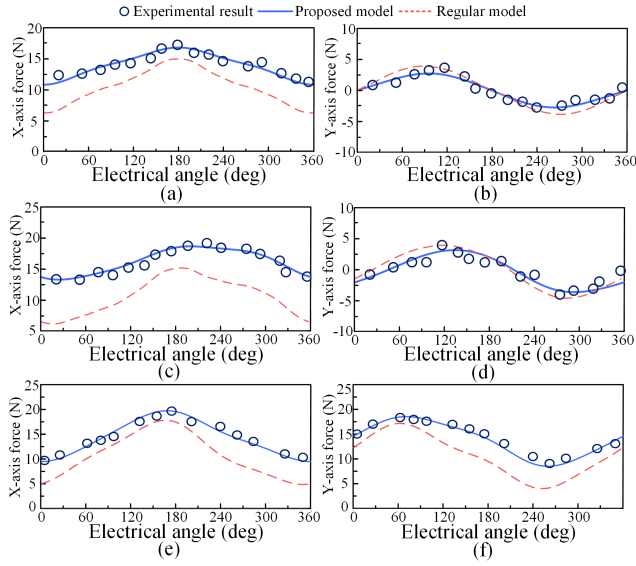


Fig. 16. Radial force measured from experiment. (a) X-axis force with $i_q=0$ A, $i_x=-3$ A, $i_y=0$ A. (b) Y-axis force with $i_q=0$ A, $i_x=-3$ A, $i_y=0$ A. (c) X-axis force with $i_q=-2$ A, $i_x=-3$ A, $i_y=0$ A. (d) Y-axis force with $i_q=-2$ A, $i_x=-3$ A, $i_y=0$ A. (e) X-axis force with $i_q=-2$ A, $i_x=-3$ A, $i_y=-3$ A. (f) Y-axis force with $i_q=-2$ A, $i_x=-3$ A, $i_y=-3$ A.

uniform.

Fig. 18 shows the rotor movements and trajectory during rotation. Additionally, the experimental results with the decoupling strategy based on the regular radial force model are presented for comparison. The speed in the experiment is 100 rpm, corresponding to a period of 0.6s, and the load current i_q is 3.0 A. The waveforms of Fig. 18 (c) and (d) exhibit a repeating cycle of 0.6s, aligning with the rotational period of the rotor. Each period encompasses ten micro-vibrations with the frequency of 16.667Hz, equaling to the electrical frequency. Via applying proposed decoupling strategy, the fluctuations in x - y axis are reduced by 44.3% and 48.5%. The max fluctuations in Fig. 18(c) are $45.8 \mu\text{m}$ and $69.7 \mu\text{m}$ in x - y axis respectively. And the max fluctuations in Fig. 18(d) are $25.5 \mu\text{m}$ and $35.9 \mu\text{m}$. Furthermore, Fig. 18(a) (b) demonstrate a good improvement in rotor vibration reduction. The machining errors of the rotor introduce difference in balanced point calibration and suspension control performance in x -axis and y -axis.

The step response of rotor movement is examined and shown in Fig. 19 to further analyze the impact of rotor displacement on the decoupled strategy control performance. Comparing the suspension control based on the regular model, the proposed model demonstrates a reduction in rotor displacement fluctuations in x - y axis by 22.4% / 33.8%, and 19.1% / 41.9% before and after the step event, respectively. The radial force-coupling effect leads to increased displacement fluctuation in the y -axis as the rotor deviates from the balanced point in the x -axis after step response happens. And the decoupling strategy effectively mitigates the interaction between the x - y axis. As depicted in Fig. 19, the response speed of the rotor movement is close across the control strategies based on different analytical model since they share the same set

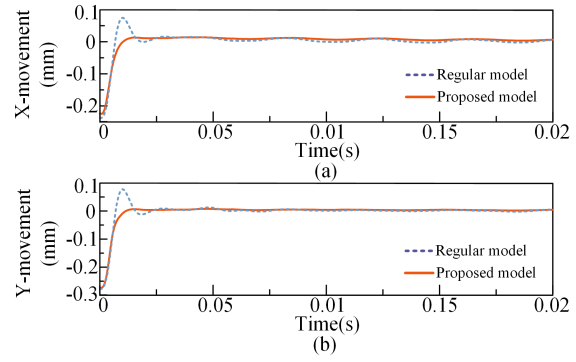


Fig. 17. The experimental results of the rotor movements during start-up procedure. (a) X-axis movement. (b) Y-axis movement.

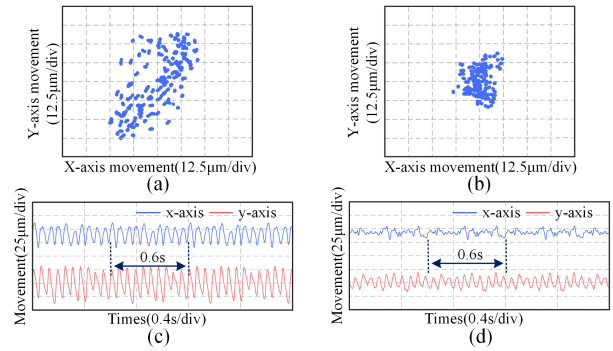


Fig. 18. Experimental results of rotor movements and trajectory. (a) Control strategy based on the regular model. (b) Control strategy based on the proposed model. (c) Control strategy based on the regular model. (d) Control strategy based on the proposed model.

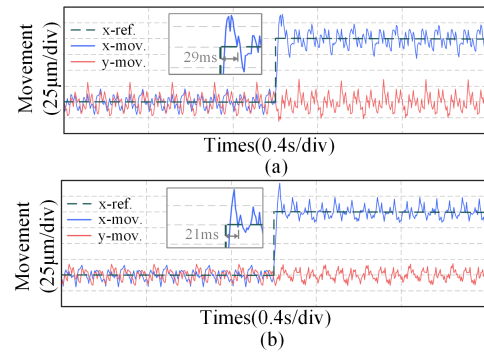


Fig. 19. Step response of rotor movements. (a) Control strategy based on the regular model. (b) Control strategy based on the proposed model.

of control parameters for the PID controller. However, the adjustment time of the strategy based on the proposed model is notably reduced compared to the strategy based on the regular model.

In Fig. 20, the suspension performance is evaluated across speeds ranging from 250 rpm to 400 rpm. During the acceleration phase, the maximum displacement fluctuations in the x - y axis with the control strategy based on the regular radial force model are $45.7 \mu\text{m}$ and $62.0 \mu\text{m}$, respectively. On the other hand, the control strategy based on the proposed model achieves maximum displacement fluctuations of 39.6

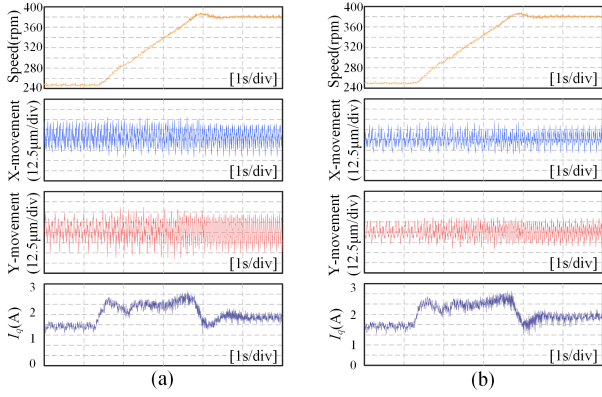


Fig. 20. Experimental results at the condition of variable speed. (a) Control strategy based on the regular model. (b) Control strategy based on the proposed model.

μm and $39.5 \mu\text{m}$ in the x - y axis. These results demonstrate the improved performance of the proposed model in reducing displacement fluctuations during acceleration.

VI. CONCLUSION

In summary, this paper introduces an advanced magnetic field model for precise calculation of the active radial force in DC-FRBLM and addresses the force-coupling issue. The proposed model incorporates a precise double-salient permeance model and accounts for leakage flux, resulting in improved accuracy compared to the regular analytical model. FEA results confirm the effectiveness of the proposed model. Additionally, the paper analyzes the fluctuation and coupling of the suspension force in the x - y axis caused by the rotating magnetic field. To mitigate rotor vibration, a decoupling strategy based on the radial force model is designed and experimentally validated. The results demonstrate the effectiveness of the decoupling strategy across various operational scenarios. In conclusion, the proposed model and decoupling strategy offer advancements in understanding and controlling DC-FRBLM, leading to improved levitation performance and reduced rotor vibration.

APPENDIX

To facilitate the derivation, two functions are defined as:

$$f_1(n_1, n_2) = \begin{cases} 1 & |n_1| = n_2 \\ 0 & \text{else} \end{cases} \quad (\text{A1})$$

$$f_c(n_1, n_2) = \cos[n_1 Z_r (\Omega t - \theta_s) \pm n_2 Z_s \theta_s] \quad (\text{A2})$$

The Fourier expansion of λ_s and λ_r is expressed as (A3).

$$\begin{cases} \lambda_s(\theta_s) = \sum_{n_s=0}^{\infty} k_s(n_s) \cos(Z_s n_s \theta_s) \\ \lambda_r(\theta_s, t) = \sum_{n_r=0}^{\infty} k_r(n_r) \cos[Z_r n_r (\Omega t - \theta_s)] \end{cases} \quad (\text{A3})$$

Then (10) can be expanded as (A4).

$$k_{sr} = 1 + \frac{k_{sr \max}}{2} \sum_{n_s=0}^{\infty} \sum_{n_r=0}^{\infty} k_s'(n_s) k_r'(n_r) f_c(n_r, n_s) \quad (\text{A4})$$

$$\begin{cases} k_s'(0) = k_s(0) - 1, k_s'(n_s) = k_s(n_s) \\ k_r'(0) = k_r(0) - 1, k_r'(n_r) = k_r(n_r) \end{cases}$$

(A5) can be obtained by substituting (A3), (A4) into (5a).

$$\begin{aligned} \Lambda &= \frac{\mu_0}{2g_0} k_{sr} \lambda_r \lambda_s = \frac{\mu_0}{2g_0} \sum_{n_s=0}^{\infty} \sum_{n_r=0}^{\infty} k_r(n_r) k_s(n_s) f_c(n_r, n_s) \\ &+ \sum_{n_{s1}=0}^{\infty} \sum_{n_{r1}=0}^{\infty} \sum_{n_{s2}=0}^{\infty} \sum_{n_{r2}=0}^{\infty} w_n f_c(n_{r1} \pm n_{r2}, n_{s1} \pm n_{s2}) \\ &= \sum_{n_s=0}^{\infty} \sum_{n_r=0}^{\infty} k_{pr}(n_r, n_s) f_c(n_r, n_s) \\ w_n &= \frac{k_{sr \max} \mu_0}{8g_0} k_r'(n_{r2}) k_s'(n_{s2}) k_r(n_{r1}) k_s(n_{s1}) \end{aligned} \quad (\text{A5})$$

$$\begin{cases} k_{pr}(n_r, n_s) = \frac{\mu_0}{2g_0} k_r(n_r) k_s(n_s) + \frac{k_{sr \min} \mu_0}{8g_0} k_r''(n_r) k_s''(n_s) \\ k_s''(n_s) = \sum_{n_{s1}=0}^{\infty} \sum_{n_{s2}=0}^{\infty} k_s'(n_{s2}) k_s(n_{s1}) f_1(n_{s1} \pm n_{s2}, n_s) \\ k_r''(n_r) = \sum_{n_{r1}=0}^{\infty} \sum_{n_{r2}=0}^{\infty} k_r'(n_{r2}) k_r(n_{r1}) f_1(n_{r1} \pm n_{r2}, n_r) \end{cases} \quad (\text{A6})$$

REFERENCES

- [1] X. Sun, L. Chen, and Z. Yang, "Overview of bearingless permanent-magnet synchronous motors," *IEEE Trans. Ind. Electron.*, vol. 60, no. 12, pp. 5528–5538, Dec 2013.
- [2] T. Pei, D. Li, J. Liu, J. Li, and W. Kong, "Review of bearingless synchronous motors: Principle and topology," *IEEE Trans. Transp. Electrification*, vol. 8, no. 3, pp. 3489–3502, Sep 2022.
- [3] T. Reichert, T. Nussbaumer, and J. W. Kolar, "Bearingless 300-w pmsm for bioreactor mixing," *IEEE Trans. Ind. Electron.*, vol. 59, no. 3, pp. 1376–1388, Mar 2012.
- [4] N. Kurita, T. Ishikawa, N. Saito, T. Masuzawa, and D. L. Timms, "A double-sided stator type axial bearingless motor development for total artificial heart," *IEEE Trans. Ind. Appl.*, vol. 55, no. 2, pp. 1516–1523, Mar/Apr 2019.
- [5] J. Chen, J. Zhu, and E. L. Severson, "Review of bearingless motor technology for significant power applications," *IEEE Trans. Ind. Appl.*, vol. 56, no. 2, pp. 1377–1388, Mar/Apr 2020.
- [6] H. Mitterhofer, W. Gruber, and W. Amrhein, "On the high speed capacity of bearingless drives," *IEEE Trans. Ind. Electron.*, vol. 61, no. 6, pp. 3119–3126, Jun 2014.
- [7] B. S. Weinreb, M. Noh, D. C. Fyler, and D. L. Trumper, "Design and implementation of a novel interior permanent magnet bearingless slice motor," *IEEE Trans. Ind. Appl.*, vol. 57, no. 6, pp. 6774–6782, Nov/Dec 2021.
- [8] J. Amemiya, A. Chiba, D. Dorrell, and T. Fukao, "Basic characteristics of a consequent-pole-type bearingless motor," *IEEE Trans. Magn.*, vol. 41, no. 1, pp. 82–89, Jan 2005.
- [9] W. Gruber, M. Rothbacher, and R. T. SchÄbb, "Design of a novel homopolar bearingless slice motor with reluctance rotor," *IEEE Trans. Ind. Appl.*, vol. 51, no. 2, pp. 1456–1464, Mar/Apr 2015.
- [10] L. Fang, D. Li, and R. Qu, "Torque improvement of vernier permanent magnet machine with larger rotor pole pairs than stator teeth number," *IEEE Trans. Ind. Electron.*, vol. 70, no. 12, pp. 12 648–12 659, Jan 2023.
- [11] W. Gruber, W. Briewasser, M. Rothbacher, and R. T. SchÄbb, "Bearingless slice motor concepts without permanent magnets in the rotor," in *Proc. IEEE Int. Conf. Ind. Technol.*, Feb 2013, pp. 259–265.
- [12] T. Pei, D. Li, J. Liu, and W. Kong, "A novel flux-reversal bearingless slice motor controlled by rotor angle independent suspension current," *IEEE Trans. Ind. Electron.*, vol. 70, no. 6, pp. 5615–5625, Jun 2023.
- [13] G. Valente, A. Formentini, L. Papini, C. Gerada, and P. Zanchetta, "Performance improvement of bearingless multisector pmsm with optimal robust position control," *IEEE Trans. Power Electron.*, vol. 34, no. 4, pp. 3575–3585, Apr 2019.
- [14] X. Cao, J. Zhou, C. Liu, and Z. Deng, "Advanced control method for a single-winding bearingless switched reluctance motor to reduce torque ripple and radial displacement," *IEEE Trans. Energy Convers.*, vol. 32, no. 4, pp. 1533–1543, Dec 2017.
- [15] Z. Yang, D. Zhang, X. Sun, and X. Ye, "Adaptive exponential sliding mode control for a bearingless induction motor based on a disturbance observer," *IEEE Access*, vol. 6, pp. 35 425–35 434, Jul 2018.

- [16] Y. Chen and Y. Zhou, "Active disturbance rejection and ripple suppression control strategy with model compensation of single-winding bearingless flux-switching permanent magnet motor," *IEEE Trans. Ind. Electron.*, vol. 69, no. 8, pp. 7708–7719, Aug 2022.
- [17] Z. Q. Zhu, L. J. Wu, and Z. P. Xia, "An accurate subdomain model for magnetic field computation in slotted surface-mounted permanent-magnet machines," *IEEE Trans. Magn.*, vol. 46, no. 4, pp. 1100–1115, Nov 2010.
- [18] Y. Zhou, F. Fang, and M. Zheng, "Research on fast design of key variables of bearingless flux-switching motor based on variable structure magnetic network," *IEEE Trans. Ind. Appl.*, vol. 55, no. 2, pp. 1372–1381, Mar/Apr 2019.
- [19] Z. Cui, Y. Zhou, J. Zhang, and W. Liu, "Modeling and analysis of dual-winding bearingless flux-switching permanent magnet motor considering magnetic saturation based on subdomain model," *IEEE Trans. Energy Convers.*, vol. 37, no. 1, pp. 132–144, Mar 2022.
- [20] J. Asama, T. Oi, T. Oiwa, and A. Chiba, "Simple driving method for a 2-dof controlled bearingless motor using one three-phase inverter," *IEEE Trans. Ind. Appl.*, vol. 54, no. 5, pp. 4365–4376, Jun 2018.
- [21] H. Wang and F. Li, "Design consideration and characteristic investigation of modular permanent magnet bearingless switched reluctance motor," *IEEE Trans. Ind. Electron.*, vol. 67, no. 6, pp. 4326–4337, Jun 2020.
- [22] L. Fang, D. Li, and Y. Zhang, "Analysis of consequent pole vernier pm machine based on advanced mmf-permeance model," in *Proc. IEEE 3rd China Int. Youth Conf. Electr. Eng. (CIYCEE)*, Nov 2022, pp. 1–6.
- [23] H. Huang, D. Li, R. Qu, X. Gao, and B. Han, "Design and analysis of t-shaped consequent pole dual pm vernier machines with differential magnetic network method," *IEEE J. Emerg. Sel. Topics Power Electron.*, vol. 10, no. 4, pp. 4546–4555, Aug 2022.